Inorganic Chemistry

pubs.acs.org/IC Article

Organic–Inorganic Hybrid Cerium-Encapsulated Selenotungstate Including Three Building Blocks and Its Electrochemical Detection of Dopamine and Paracetamol

Jun Jiang, Lulu Liu, Guoping Liu, Dan Wang, Yan Zhang, Lijuan Chen,* and Junwei Zhao*

Cite This: *Inorg. Chem.* 2020, 59, 15355–15364 Read Online

ACCESS | Metrics & More | Article Recommendations | Supporting Information

ABSTRACT: A novel organic–inorganic hybrid cerium-encapsulated selenotungstate comprising three polyoxotungstate building units $Na_{16}H_6\{[Ce_3W_4O_{10}(H_2O)_9(CH_3COO)_3]_2(Se_2W_7O_{30})(B\text{-}\alpha\text{-}SeW_9O_{33})_4\}\cdot(C_5H_8NBO_3)\cdot 119H_2O$ (**1**) was synthesized by the portfolio approach of an in situ self-assembly reaction and step-by-step synthesis. The hybrid polyoxoanion of **1** is constructed from an acetate-coordinated heterometallic $\{[(Ce_3W_4O_{10})(H_2O)_9(CH_3COO)_3]_2(Se_2W_7O_{30})\}^{10+}$ core encompassing four trilacunary $[B\text{-}\alpha\text{-}SeW_9O_{33}]^{8-}$ subunits. Interestingly, the heterometallic core contains a remarkable $[Se_2W_7O_{30}]^{10-}$ building block in which seven W^{VI} atoms form a W_7 plane and two Se^{IV} atoms are situated on two opposite faces of the W_7 plane. In addition, the electrochemical performances of the **1**@CFMCN composite (CFMCN: carboxyl-functionalized multiwalled carbon nanotube) were investigated. The **1**@CFMCN/GCE (GCE: glass carbon electrode) sensor demonstrates a promising potential in electrochemically sensing dopamine (DPA) or paracetamol (PCM) or even simultaneously detecting DPA and PCM with low limits of 0.053 μM for DPA and 2.03 μM for PCM over a wide linear range at high sensitivity.

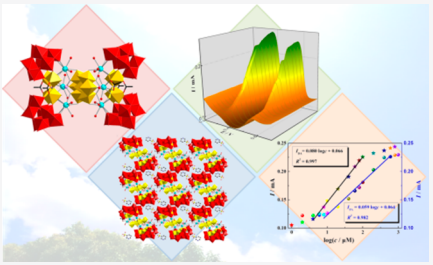

INTRODUCTION

Polyoxometalates (POMs) are extraordinary kinds of metal–oxygen anionic clusters composed of high-oxidation-state early transition metals (typically Mo^{VI}, W^{VI}, V^{V}, Nb^{V}, and Ta^{V}) with not only glamorous structures but also application prospects in catalysis, optics, magnetism, materials science, and so on.[1−5] The key to building POMs is the type of heteroatom, which determines the structures of polyoxoanions and exhibits some particular traits.[6−8] To date, most available POMs are based on conventional tetrahedral heteroatoms such as Si^{IV}, P^{IV}, and Ge^{IV}.[9−11] However, with the deepening and expanding study on POMs, the pyramidal heteroatoms containing lone-pair electrons (e.g., As^{III}, Sb^{III}, Bi^{III}, Se^{IV}, and Te^{IV}) have aroused increasing concern.[12−14] In contrast to the tetrahedral heteroatoms, the most distinct advantage of heteroatoms containing lone-pair electrons is that the steric effect caused by lone-pair electrons could prevent the formation of saturated Keggin POMs, and it is also means that lacunary POM fragments could be directly generated without presynthesized precursors.[15] The vacant POM fragments could self-assemble into high-nuclearity clusters or coordinate with other transition-metal (TM) or lanthanide (Ln) ions to derive various POMs.[16] In addition, a growing amount of research has confirmed that pyramidal XO_3^{2-} (X = As^{III}, Sb^{III}, Bi^{III}, Se^{IV}, Te^{IV}, etc.) could be used as a linker to bridge POM fragments and/or other metal centers, thus manufacturing a variety of structures.[17−19]

Selenotungstates (SeTs), as an important subset of POMs, have been rapidly developed in the past decade. The Se^{IV} heteroatom contains a pair of lone electrons, so the pyramidal SeO_3^{2-} group can serve as a template for constructing POM-based open-framework SeTs and further concatenating with different sorts of metals to form diverse structures. Earlier studies (before 2016) were focused on the "pure" SeTs and TM-substituted SeTs.[20−30] In the last decade, Ln-containing POMs have drawn incremental attention on account of the excellent luminescence properties of Ln cations.[31,32] Compared with TM ions, Ln ions have abundant coordination modes and intense oxophilicity, making it easy for them to capture lacunary POM fragments to expand structural diversity.[33−37] In the last 5 years, research has been focused on Ln-substituted SeTs (LnSSeTs).[38−46] The first LnSSeTs are the octameric nanoclusters reported by Su's group, which could be self-assembled to hollow spheres in dilute solution, and the electrochemical and magnetic properties of these LnSSeTs were investigated.[38] We have devoted ourselves to synthesizing LnSeSTs and achieved some prominent results.[42−46] Typically, trimeric and hexameric LnSSeTs have

Received: August 4, 2020
Published: October 1, 2020

https://dx.doi.org/10.1021/acs.inorgchem.0c02318
Inorg. Chem. 2020, 59, 15355–15364

been isolated in the presence of different organocations. Their catalytic performances were also investigated, and the results showed that they can triumphantly catalyze the oxidation of aromatic sulfides by H_2O_2.[44] Last year, we published the penta-Ln-cluster including Dawson-type SeTs, which were also used to produce surfactant-functionalized nanosized materials, and their fluorescence properties were systematically explored.[46]

Through reviewing the related literature on LnSSeTs, we can summarize the following features. Almost all of the reported LnSSeTs were prepared by the one-step self-assembly method, and in this flexible reaction environment, the template effect of SeO_3^{2-} can prompt simple tungstates to directly aggregate into SeT building blocks and then combine with Ln cations to form fascinating and multifarious LnSSeTs. These structures have the commonality that they all consist of one kind of SeT building blocks and some isopolyoxotungstate fragments. However, it is rare to find LnSSeTs including two or more kinds of SeT building blocks. On one hand, under a background of developing organic−inorganic hybrid materials, organic-ligand-functionalized POMs are gradually flourishing. Nearly all of the LnSSeTs are purely inorganic, while organic-ligand-functionalized LnSSeTs are extremely rare. Thus, this background provides a good chance to discover novel organic−inorganic hybrid LnSSeTs containing multiple and neoteric SeT building blocks. Obviously, the conventional one-step self-assembly method in aqueous solution could not meet the above demands, so the mixed solvent method comes into sight. Acetic acid (HAc), as an organic solvent, can be miscible with water and can improve the solubility of organic ligands in the reaction system, which boosts the possibility of coordination between organic ligands and POM segments. Moreover, HAc could adjust the pH value of the whole reaction system as an appropriate acidity regulator. More importantly, HAc has a carboxyl group and has a great coordination ability with various metals. On the other hand, the portfolio approach of the in situ self-assembly reaction in mixed solvent and step-by-step synthesis is introduced into the reaction system. In the HAc−NaAc buffer solution, tungstate reacts with selenite to in situ generate SeT building blocks. The glacial acetic acid is used to dissolve Ln salts and organic components. Finally, two solutions are mixed to prepare our desired organic−inorganic hybrid LnSSeTs under heating. On the basis of these thoughts, we obtained an organic−inorganic hybrid Ce^{III}-encapsulated SeT $Na_{16}H_6\{[Ce_3W_4O_{10}(H_2O)_9(CH_3COO)_3]_2(Se_2W_7O_{30})(B\text{-}\alpha\text{-}SeW_9O_{33})_4\}\cdot(C_5H_8NBO_3)\cdot 119H_2O$ (**1**). Noticeably, the fascinating $[Se_2W_7O_{30}]^{10-}$ building block is sparsely encountered, in which seven W^{VI} atoms form a dumbbell-shaped W_7 plane. Evidently, the structure of **1** comprises three kinds of POM building blocks, namely, $[Ce_3W_4O_{10}]^{13+}$, $[Se_2W_7O_{30}]^{10-}$, and $[B\text{-}\alpha\text{-}SeW_9O_{33}]^{8-}$, which to some degree indicates that the portfolio approach of the in situ self-assembly reaction in mixed solvent and step-by-step synthesis has a great potential in constructing complicated and multicomponent poly(POM) aggregates containing two or more types of POM building blocks. In addition, **1** was loaded on CFMCN to produce the **1**@CFMCN composite, which can be utilized as a **1**@CFMCN/GCE electrochemical sensor (ECS) to detect dopamine (DPA) and paracetamol (PCM). The results illustrate that this ECS exhibits outstanding detection performance toward DPA, PCM, and both of them simultaneously with low limits of detection of 0.053 μM for DPA and 2.03 μM for PCM in the linear range of 4−100 μM for DPA and 8−600 μM for PCM.

RESULTS AND DISCUSSION

Synthesis. Almost all the reported LnSSeTs were synthesized by the one-step self-assembly method in water. To obtain the innovative LnSSeTs including two or more kinds of SeT building blocks, the new synthesis strategy should be applied. Therefore, **1** was synthesized via the portfolio approach of an in situ self-assembly reaction in mixed solvent and step-by-step synthesis based on simple raw materials $Na_2WO_4\cdot 2H_2O$, Na_2SeO_3, $Ce(NO_3)_3\cdot 6H_2O$, and 3-pyridinylboronic acid (Figure 1). First, some documents prove that

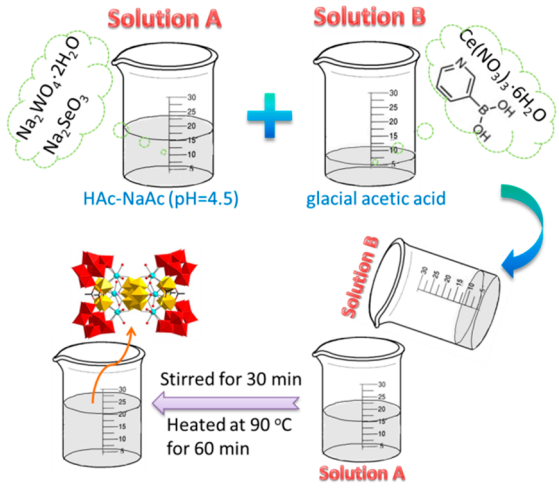

Figure 1. Schematic synthesis route for **1**.

various SeT building blocks could be straightforwardly formed in the pH range of 3.0−5.0, so in the synthesis process, the 0.2 M NaAc−HAc buffer solution provided an acidic context (pH 4.5) for $Na_2WO_4\cdot 2H_2O$ and Na_2SeO_3, which would facilitate to the in situ formation of SeT building blocks. Second, HAc not only works as the acidity regulator of the whole reaction process, but also functions as the solvent for 3-pyridinylboronic acid. 3-Pyridinylboronic acid should be first dissolved in glacial acetic acid together with $Ce(NO_3)_3\cdot 6H_2O$, followed by being poured into the A reaction system. If 3-pyridinylboronic acid was directly added to the A reaction system, then the reaction solution became turbid and could become clear again. Similarly, if $Ce(NO_3)_3\cdot 6H_2O$ was directly added to the A solution, then the solution rapidly became turbid because of the hydrolyzation of Ce^{3+} cations. Hence, $Ce(NO_3)_3\cdot 6H_2O$ was dissolved in glacial acetic acid, which also increased the chance of coordination between Ce^{3+} cations and acetate. Third, the A and B solutions were mingled, and in this step, Ce^{3+} cations bridged the in-situ-generated SeT building blocks to build organic−inorganic hybrid Ce^{III}-encapsulated SeT **1**. Additionally, 3-pyridinylboronic acids work as fillers in the space packing of polyoxoanions (POAs) of **1** to reduce steric hindrance. The final pH of the reaction was also very critical in the production of **1**. Experimental results showed that 3.90 was the best pH for crystal growth when a few drops of HAc were replenished in the mixed reaction system. In addition, when other Ln cations were used to replace Ce^{3+} cations, no similar species have been formed to date, which may be related to the certain particularity of Ce^{3+} cations in this reaction system, and this phenomenon has also appeared in the literature.[38,47,48]

https://dx.doi.org/10.1021/acs.inorgchem.0c02318
Inorg. Chem. 2020, 59, 15355−15364

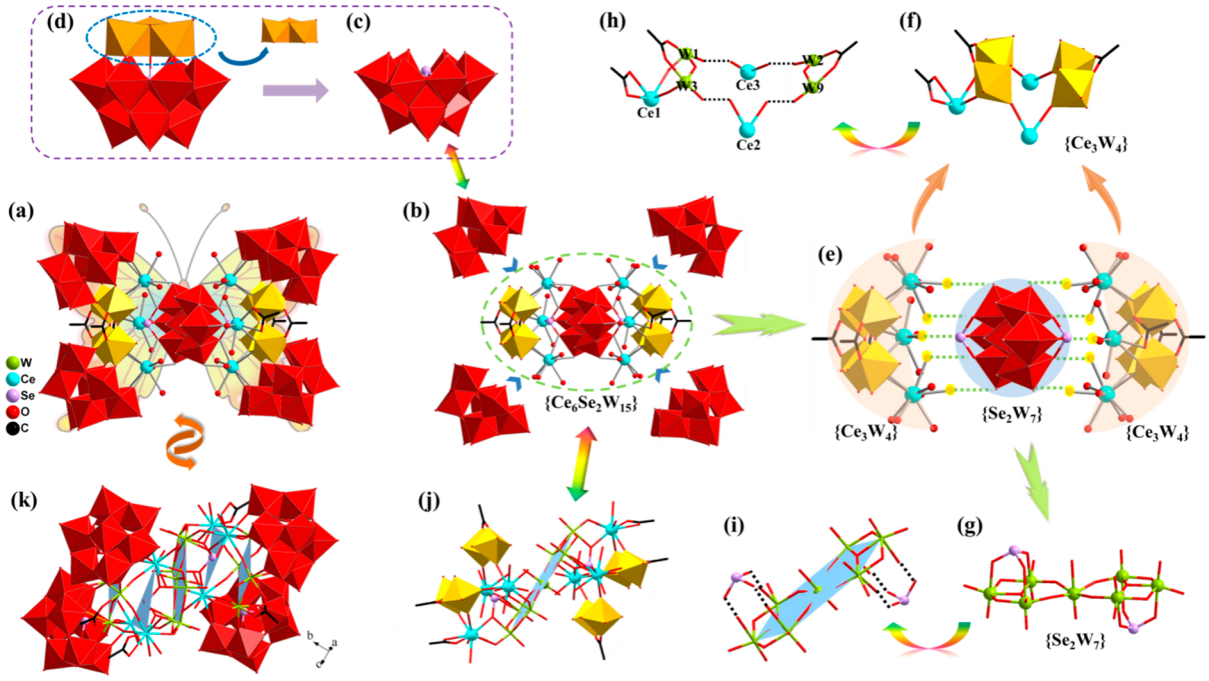

Figure 2. (a) POA of **1**. (b) Combination of the $\{Ce_6Se_2W_{15}\}$ heterometal cluster and four trilacunary $[B\text{-}\alpha\text{-}SeW_9O_{33}]^{8-}$ segments in **1**. (c) View of the $[B\text{-}\alpha\text{-}SeW_9O_{33}]^{8-}$ segment. (d) View of the hypothetical plenary Keggin-type $[SeW_{12}O_{40}]^{4-}$ POA. (e) Connection mode between two $\{Ce_3W_4\}$ subunits and a $\{Se_2W_7\}$ subunit in the $\{Ce_6Se_2W_{15}\}$ heterometal cluster. (f) View of the $\{Ce_3W_4\}$ subunit. (g) View of the $\{Se_2W_7\}$ subunit. (h) Connection mode in the $\{Ce_3W_4\}$ subunit. (i) Connection mode between two Se ions and the W7 plane in the $\{Se_2W_7\}$ subunit. (j) View of the $\{Ce_6Se_2W_{15}\}$ heterometal cluster. (k) View of the POA skeleton for **1** viewed along the *a* axis. W, bright green; C, black; N, blue; O, red; Ce, turquoise; Se, lavender; $\{WO_6\}$, red and yellow.

Structural Discussion. The pure phase of **1** has been identified by powder X-ray diffraction (Figure S1). It crystallizes in monoclinic space group $P\bar{1}$ (Table S1). The molecular unit of **1** is composed of 1 tetrameric $\{[(Ce_3W_4O_{10})(H_2O)_9(CH_3COO)_3]_2(Se_2W_7O_{30})(B\text{-}\alpha\text{-}SeW_9O_{33})_4\}^{22-}$ POA (Figure 2a), 1 $C_5H_8NBO_3$ zwitterion (Figure S2), 16 Na^+ cations, and 119 lattice water molecules. It should be pointed out that the POA of **1** is composed of a Ce−W−Se heterometal cluster $\{[(Ce_3W_4O_{10})(H_2O)_9(CH_3COO)_3]_2(Se_2W_7O_{30})\}^{10+}$ ($\{Ce_6Se_2W_{15}\}$) surrounded by four trilacunary $[B\text{-}\alpha\text{-}SeW_9O_{33}]^{8-}$ segments (Figure 2b). The trilacunary $[B\text{-}\alpha\text{-}SeW_9O_{33}]^{8-}$ segment (Figure 2c) can be seen as the remainder of the hypothetical plenary Keggin-type $[SeW_{12}O_{40}]^{4-}$ (Figure 2d) by removal of an edge-sharing $\{W_3O_{13}\}$ triad. The special $\{Ce_6Se_2W_{15}\}$ heterometal cluster (Figure 2e) consists of 2 $[(Ce_3W_4O_{10})(H_2O)_9(CH_3COO)_3]^{10+}$ ($\{Ce_3W_4\}$) subunits (Figure 2f) and 1 $[Se_2W_7O_{30}]^{10-}$ ($\{Se_2W_7\}$) subunit (Figure 2g) through 10 oxygen atoms. In the $\{Ce_3W_4\}$ subunit, $Ce2^{3+}$ and $Ce3^{3+}$ ions connect two $\{W_2O_{11}\}$ fragments and the Ce1 ion chelated by one acetate group is suspended on one $\{W_2O_{11}\}$ cluster through linking W1 and W3 together (Figure 2h). Also, two W centers in each $\{W_2O_{11}\}$ cluster are bridged by one acetate group. Three crystallographically independent Ce^{3+} cations ($Ce1^{3+}$, $Ce2^{3+}$, and $Ce3^{3+}$) in $\{Ce_3W_4\}$ all employ severely contorted monocapped square antiprism geometry (Figure S3a−c). The $Ce1^{3+}$ cation binds to the $\{Se_2W_7\}$ unit by two O atoms (O64, O53) and to one $\{W_2O_{11}\}$ group by two O atoms (O26, O59) [Ce−O: 2.436(11)−2.628(10) Å], together with one acetate group [Ce−O: 2.548(13)−2.559(13) Å] and three water molecules [Ce−O: 2.509(14)−2.556(11) Å]. $Ce2^{3+}$ and $Ce3^{3+}$ cations link two $\{W_2O_{11}\}$ clusters by four O atoms and one $[B\text{-}\alpha\text{-}SeW_9O_{33}]^{8-}$ segment by two O atoms [Ce−O: 2.461(13)−2.617(10) Å] as well as three water molecules [Ce−O: 2.504(11)−2.621(12) Å] (Figure S3a−c). Surprisingly, in the specific $\{Se_2W_7\}$ building block, the central W atom and two triangular triads formed by three edge-sharing $\{WO_6\}$ octahedra are aligned in the dumbbell-shaped motif and the seven W atoms are approximately situated in the same plane (W_7 plane) (Figure 2i). Opposite faces of the W_7 plane are capped by two Se^{IV} atoms in the asymmetical motif (Figure 2i), and the distance between the Se^{IV} atom and the W_7 plane is 3.011 Å. Therefore, two $\{Ce_3W_4\}$ subunits are located on the two faces of the central $\{Se_2W_7\}$ unit by linking Ce^{3+} ions and the $\{Se_2W_7\}$ group to form the heterometal $\{Ce_6Se_2W_{15}\}$ cluster core (Figure 2j). In this direction, there are five planes: one W_7 plane is in the center, two planes arranged by six Ce^{3+} cations are in the mezzanine, and two planes defined by eight W atoms are on the surface (Figure 2k). These planes are substantially parallel, and the heterometal $\{Ce_6Se_2W_{15}\}$ cluster core is centered on the W7 plane to make up a misaligned sandwich formation. Overall, the POA of **1** is fabricated from three kinds of building blocks, namely, four trilacunary Kiggin-type $[B\text{-}\alpha\text{-}SeW_9O_{33}]^{8-}$ fragments, two acetate-coordinated heterometallic $\{Ce_3W_4\}$ units, and an extraordinary $\{Se_2W_7\}$ segment.

In POM chemistry, $\{X_nW_7\}$ (n = 0, 1, 2) building blocks are uncommon compared with saturated Keggin $\{XW_{12}\}$, monovacant $\{XW_{11}\}$, divacant $\{XW_{10}\}$, and trivacant $\{XW_9\}$ segments. For example, the pentavacant Keggin $[B\text{-}\alpha\text{-}TeW_7O_{28}]^{10-}$ segment in $[Ln_2(OH)(B\text{-}\alpha\text{-}TeW_7O_{28})Sn_2(CH_3)_4(W_5O_{18})]_2^{14-}$ is derived from the classical trivacant $[B\text{-}\alpha\text{-}TeW_9O_{33}]^{8-}$ fragments by eliding an edge-sharing $\{W_2O_{10}\}$ subunit (Figure 3a).[49] The $[XW_7O_{28}]^{10-}$ (X = As^{III},

https://dx.doi.org/10.1021/acs.inorgchem.0c02318
Inorg. Chem. 2020, 59, 15355−15364

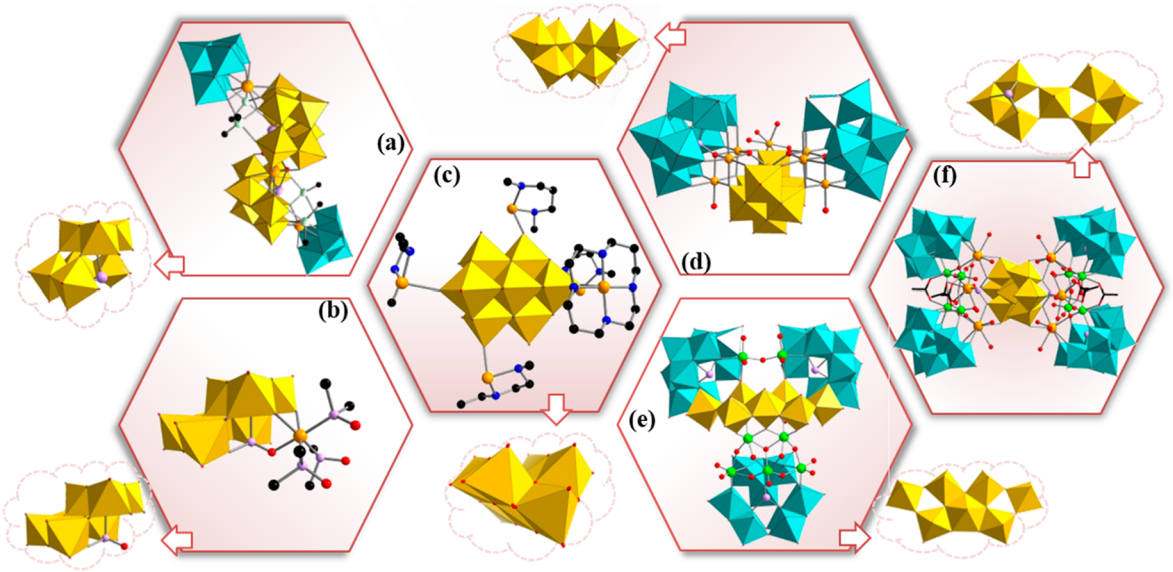

Figure 3. (a) Pentavacant Keggin $[B\text{-}\alpha\text{-}TeW_7O_{28}]^{10-}$ segment in $[Ln_2(OH)(B\text{-}\alpha\text{-}TeW_7O_{28})Sn_2(CH_3)_4(W_5O_{18})]_2^{14-}$. (b) $[XW_7O_{28}]^{10-}$ (X = As^{III}, P^{III}) segment in $[HXW_7O_{28}Ru(dmso)_3]^{6-}$ (X = As^{III}, P^{III}). (c) Paratungstate $[W_7O_{24}]^{6-}$ segment in $\{Cu(cyclam)\}_3(W_7O_{24})$. (d) V-shaped $(W_7O_{26})^{10-}$ unit in $[Co_7(H_2O)_2(OH)_2P_2W_{25}O_{94}]^{16-}$. (e) Planar $\{W_7\}$ unit in $[H_2W_{43}Se_3O_{148}]^{24-}$. (f) $\{Se_2W_7\}$ building block in **1**.

P^{III}) segment in $[HXW_7O_{28}Ru(dmso)_3]^{6-}$ is different from $[B\text{-}\alpha\text{-}TeW_7O_{28}]^{10-}$, which is considered to be a fusion of a $\{W_3O_{13}\}$ triad and an edge-sharing half-round $\{W_4O_{18}\}$ quad through a corner-sharing motif together with a $\{XO_3\}$ linker (Figure 3b).[50] The V-shaped heptatungstate $[W_7O_{24}]^{6-}$ segment in $\{Cu(cyclam)\}_3(W_7O_{24})$ can be seen as a central $\{WO_6\}$ octahedron connecting a cricoid hexamer around it by the edge-sharing mode (Figure 3c).[51] In addition, there were two $\{W_7\}$ building blocks similar to that observed in **1**. One is the V-shaped $[W_7O_{26}]^{10-}$ segment in $[Co_7(H_2O)_2(OH)_2P_2W_{25}O_{94}]^{16-}$ that can be looked on as a derivative of a hexavacant α-Keggin $\{W_6O_{22}\}$ unit capped by a $\{WO_6\}$ group in the central cavity between two $\{W_3O_{13}\}$ triads by an edge-sharing mode (Figure 3d, Figure S4a) in which the hexavacant α-Keggin $\{W_6O_{22}\}$ unit can be seen as a product of the trivacant B-α-Keggin $\{W_9O_{33}\}$ fragment by elimating one $\{W_3O_{13}\}$ triad.[52] In the V-shaped $[W_7O_{26}]^{10-}$ segment, the two $\{W_3O_{13}\}$ triads are respectively seated at two planes with a dihedral angle of 79.52° (Figure S4a). The other is the planar $\{W_7\}$ unit in $[H_2W_{43}Se_3O_{148}]^{24-}$ that is composed of a central pentagonal $\{WO_7\}$ subunit and two vertex-sharing $\{W_3O_{21}\}$ groups linked together in the edge-sharing style (Figure 3e, Figure S4b).[22] In this planar $\{W_7\}$ unit, the angle of two terminal W atoms and the central W atom is 142.41° (Figure S4b). In this article, seven W atoms in the special $\{Se_2W_7\}$ building block form one dumbbell-shaped plane, and the terminal and central W atoms were located in a straight line (Figure 3e, Figure S4b). So this dumbbell-shaped W_7 plane is significantly different from other $\{W_7\}$ building blocks.

It is noticeable that in this work acetate groups as organic constituents modify the POA structure of **1**. Among them, acetate groups can be coordinated with not only the $Ce1^{3+}$ cation, but also two W centers in each $\{W_2O_{11}\}$ unit because of the appropriate location and steric hindrance.[39,40] Above all, two acetate groups as linkers combine two adjoining W atoms. Such a phenomenon in which an acetate group directly bridges two W centers is unusual in POM chemistry, which provides a great likelihood of constructing carboxyl bridging polyoxotungstates and gives us extreme enlightenment and a high level of inspiration to expore and fabricate novel carboxylated POMs by selecting appropriate organic carboxylic acid ligands. In addition, it is fascinating that $C_5H_8NBO_3$ zwitterions exist around the POAs of **1**, which are formed by 3-pyridinylboronic acid combining a hydroxy group from aqueous solution.[53] Besides, Na^+ as a counter cation for charge balance and lattice water molecules are necessary and could interact with POAs of **1** to generate the 3D supramolecular structure. If each POA of **1** is simplified as a parallelogram using Se2, Se3, Se2A, and Se3A (Figure S5a), then spatial packing architectures for POAs of **1** could be more easily understood. Packing structures for POAs of **1** along the *a*, *b*, and *c* axes all manifest the −AAA− arrangement (Figure S5b−d), and their corresponding simplified packing architectures are shown in Figure S5e−g. If $C_5H_8NBO_3$ zwitterions are added to the 3D packing structure of **1**, then it is clear that $C_5H_8NBO_3$ zwitterions exist in intervals between the POAs of **1** (Figure S6).

Electrochemical Properties. Electrochemical sensing investigations on small biomolecules and drug molecules have brought about heightened concern owing to the quick response, low toxicity, broad linearity, and high sensitivity and selectivity.[54,55] Among them, electrode materials play a considerable role in signal enhancement. Carbon nanomaterials can be considered to be a class of excellent electrode materials due to their high electrical conductivity and stability, nanosize, and biocompatibility,[56,57] but in practice, the shortcomings of carbon nanomaterials should not be ignored, such as easy agglomeration and a weak response to target objects.[58] In fact, POMs can donate and accept electrons without structural variation, and this reversible charge-transfer ability enables them to serve as candidates for electron exchange reactions.[59] Many POMs could not be used directly as electrode materials for detection in aqueous solution due to their solubility. Therefore, the effective way to produce electrode materials is to load POMs on the carbon nanomaterials. On one hand, the responses of POM-loaded carbon-nanomaterial-modified electrodes to the testing samples can be significantly improved. On the other hand, POM-loaded carbon nanomaterials could be dispersed in aqueous solution

https://dx.doi.org/10.1021/acs.inorgchem.0c02318
Inorg. Chem. 2020, 59, 15355−15364

to get a homogeneous, stable suspension. Thus, along with these ideas, we utilize the as-synthesized **1**-loaded CFMCN as the electrode material for fabricating **1**@CFMCN/GCE ECS. The SEM image of **1**@CFMCN and energy-dispersive spectroscopy (EDS) patterns of CFMCN and **1**@CFMCN have been obtained. The appearance of W and Ce elements in the **1**@CFMCN material confirms that **1** has been loaded onto CFMCN (Figure S7).

As is known, DPA, as the most plentiful form of catecholamine neurotransmitters in the human brain, is vital for regulating and controlling the central nervous system.[60,61] The abnormal synthesis, parasecretion, and dysfunction of DPA are associated with Parkinson's disease, depression, Huntingdon's disease, and drug dependence.[62,63] PCM, also known as acetaminophen, is a common analgesic and febrifuge drug that could be used in place of aspirin when patients are allergic to and intolerant of aspirin. However, a PCM overdose would influence the sympathetic nervous system and cause life-threatening liver damage. Therefore, the detection of DPA and PCM is crucial to the diagnosis and treatment of related diseases. Meanwhile, in *in vivo* studies, the long-term ingestion of PCM probably affects the level of DPA, so the simultaneous detection of DPA and PCM is conducive to understanding the clinical significance and determining the pharmaceutical dosage.[64,65] In this article, the electrochemical responses of **1**@CFMCN/GCE ECS for DPA and PCM detection were systematically investigated. In this process, DPA and PCM could be easily electro-oxidized into their corresponding oxides as follows (Scheme 1) so that they can be detected successfully.[64]

Scheme 1. Electrochemical Oxidation and Reduction Processes of DPA and PCM

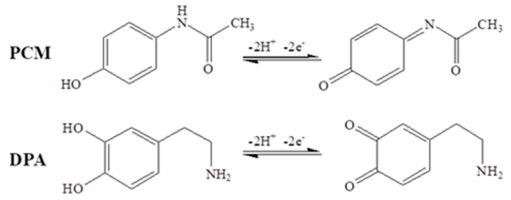

The electrochemical activities of the bare GCE and modified GCEs were examined via cyclic voltammetry (CV). Figure 4a depicts the CV curves of bare GCE, CFMCN/GCE, and **1**@CFMCN/GCE in a 5.00 mM $[Fe(CN)_6]^{4-}/[Fe(CN)_6]^{3-}$ solution. The CV curve of the bare GCE displays a peak separation (ΔE_P) of 0.093 V, indicating the good reversibility of the bare GCE. Moreover, modified CFMCN/GCE and **1**@CFMCN/GCE also have good reversibility. It can also be observed that the anode peak current rises from 0.118 to 0.164 mA after CFMCN is used to cover the bare GCE surface. After the GCE surface is coated with **1**@CFMCN, the peak current increases to 0.180 mA. Meanwhile, the ΔE_P values of these electrodes are almost invariant. Overall, it is illustrated that the **1**@CFMCN material promotes electron transport from $[Fe(CN)_6]^{4-}/[Fe(CN)_6]^{3-}$ to the electrode surface. The results described above also demonstrate that **1**, after being loaded onto CFMCN, could promote electron transport and improve the electrochemical responses. This role of POMs as electrode materials was also proven previously.[66−68]

To determine whether the **1**@CFMCN electrode material can be utilized to detect DPA and PCM, **1**@CFMCN/GCE ECS was prepared to test electrical signals in 50 mL of 0.1 M NaH_2PO_4−Na_2HPO_4 solution with/without DPA (c = 500 μM) and/or PCM (c = 500 μM). A pair of redox peaks at $E_{1/2}$ = 0.391 V ascribed to DPA in the presence of DPA (Figure S8a) and a pair of redox peaks at $E_{1/2}$ = 0.585 V ascribed to PCM in the presence of PCM (Figure S8b) are visible. In the NaH_2PO_4−Na_2HPO_4 solution containing both DPA and PCM, two redox peak signals could be explicitly seen and completely distinguished (Figure 4b, Figure S8c), which indicates that the **1**@CFMCN/GCE ECS could be used to simultaneously detect DPA and PCM. In order to validate the high activity of the **1**@CFMCN material in the detection of DPA and PCM, the differential pulse voltammetry (DPV) method was also utilized to evaluate CFMCN/GCE and **1**@CFMCN/GCE to compare their signal response strengths for detecting DPA or/and PCM. The DPV peak currents of individual DPA or PCM increase in turn in the order of bare GCE, CFMCN/GCE, and **1**@CFMCN/GCE (Figure S9a,b). In NaH_2PO_4−Na_2HPO_4 buffer solution with DPA (c = 500 μM) and PCM (c = 500 μM), this phenomenon still exists, which testifies to the good electrochemical activity of **1**@CFMCN/GCE (Figure 4c, Figure S9c). Also, the separation of peak potentials between DPA and PCM (ΔE) for CFMCN/GCE ECS (0.190 V) and **1**@CFMCN/GCE ECS (0.181 V) is much larger than that for the bare GCE (0.169 V), demonstrating that **1**@CFMCN/GCE ECS is a promising candidate for the electrochemical detection of DPA and PCM (Figure 4c).

According to the literature, the utility of an electrode materals is primarily in selecting the appropriate pH value of the solution, so the influence of pH on **1**@CFMCN/GCE ECS was investigated in 0.10 M NaH_2PO_4−Na_2HPO_4 solution with DPA and PCM (Figure S10). As shown in Figure S10a,b, the reduction and oxidation peak potentials have blue shifts with the decrease in the pH value. Within the whole scope of pH values, the current signals of DPA and PCM could be accurately distinguished, so the current peak values can be used as the selection criteria for searching the optimum pH value. When the pH value is increased from 1.0 to 6.0 (Figure 4d), the oxidation peak current of DPA gradually declines and rises a little at pH 7.0, and then it continues to decline in an alkaline environment. The oxidation peak current of PCM increases at first and then decreases with an increase in the pH value. After a comprehensive consideration, the optimum pH scope is 3.0−4.0. Nevertheless, it is necessary to investigate the structural stability of the POA skeleton of **1** in this pH scope. Therefore, the stability of the POA skeleton of **1** was probed by UV−vis spectra, and the results reveal that the POA skeleton of **1** is stable in the pH range of 3.0−8.0 (Figure S11). Considering the above-mentioned analysis, the optimum pH value is 3.0, and the following measurements were all obtained in pH 3.0 NaH_2PO_4−Na_2HPO_4 solution. Under this condition, the electrochemical stability of the **1**@CFMCN/GCE ECS was surveyed via CV for 100 cycles (Figure 4e, Figure S12). It is obvious that almost all of the CV curves overlap with each other and the slight damping of DPA and PCM peak currents can be ignored. It can be concluded that the **1**@CFMCN/GCE ECS possesses high stability, which can completely meet the experimental requirement.

The influence of the scan rate on the redox peak currents of DPA and PCM for the **1**@CFMCN/GCE ECS was also examined (Figure 4f, Figure S13). On one hand, when the scan rate increases from 20 to 180 mV/s, the cathodic peak

https://dx.doi.org/10.1021/acs.inorgchem.0c02318
Inorg. Chem. 2020, 59, 15355−15364

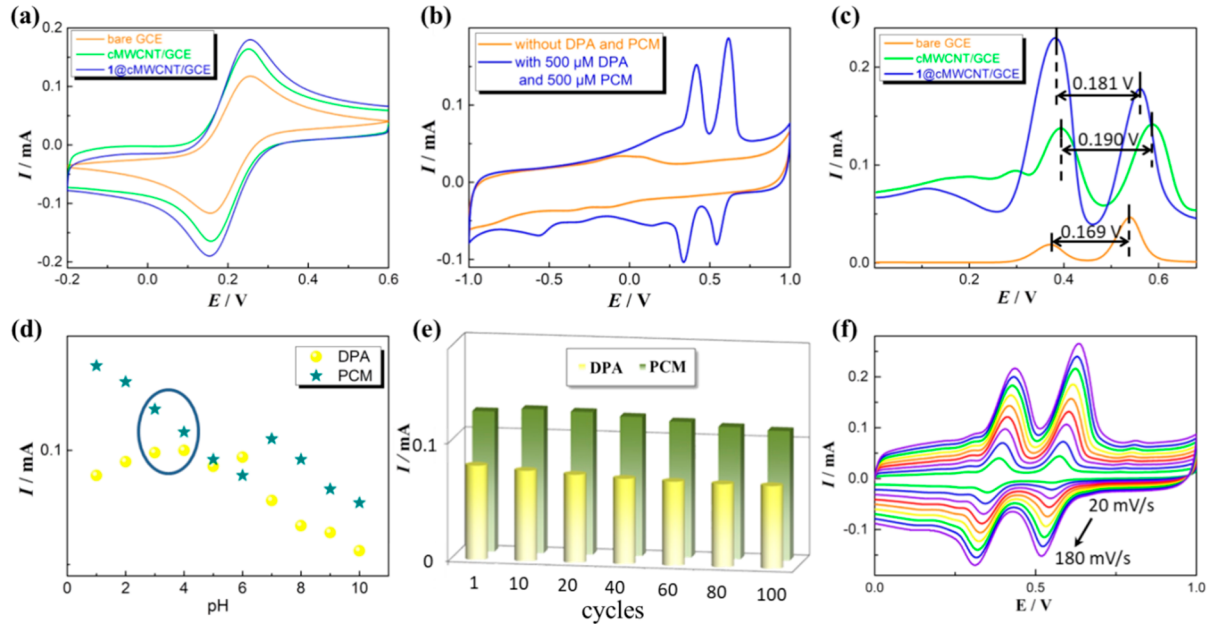

Figure 4. (a) CV curves of bare/GCE, CFMCN/GCE, and **1**@CFMCN/GCE in 5 mM $[Fe(CN)_6]^{4-}/[Fe(CN)_6]^{3-}$ solution at a scan rate of 100 mV/s. (b) Comparison of the CVs of **1**@CFMCN/GCE in 0.10 M NaH_2PO_4–Na_2HPO_4 solution (pH 3.00) with both DPA (500 μM) and PCM (500 μM) and without DPA and PCM. (c) DPV curves of bare/GCE, CFMCN/GCE, and **1**@CFMCN/GCE in a 0.10 M NaH_2PO_4–Na_2HPO_4 solution (pH 3.00) with 500 μM DPA and 500 μM PCM. (d) Anodic peak currents from CVs on **1**@CFMCN/GCE in different pH values of 0.10 M NaH_2PO_4–Na_2HPO_4 solution with 500 μM DPA and 500 μM PCM (scan rate: 100 mV/s). (e) Anodic peak currents of CVs on **1**@CFMCN/GCE ECS from the 1st to the 100th cycle in 0.10 M NaH_2PO_4–Na_2HPO_4 solution with 500 μM DA and 500 μM PA (scan rate: 100 mV/s). (f) CVs of **1**@CFMCN/GCE at different scan rates (from 20 to 180 mV/s) in 0.10 M NaH_2PO_4–Na_2HPO_4 solution (pH 3.00) with 500 μM DPA and 500 μM PCM.

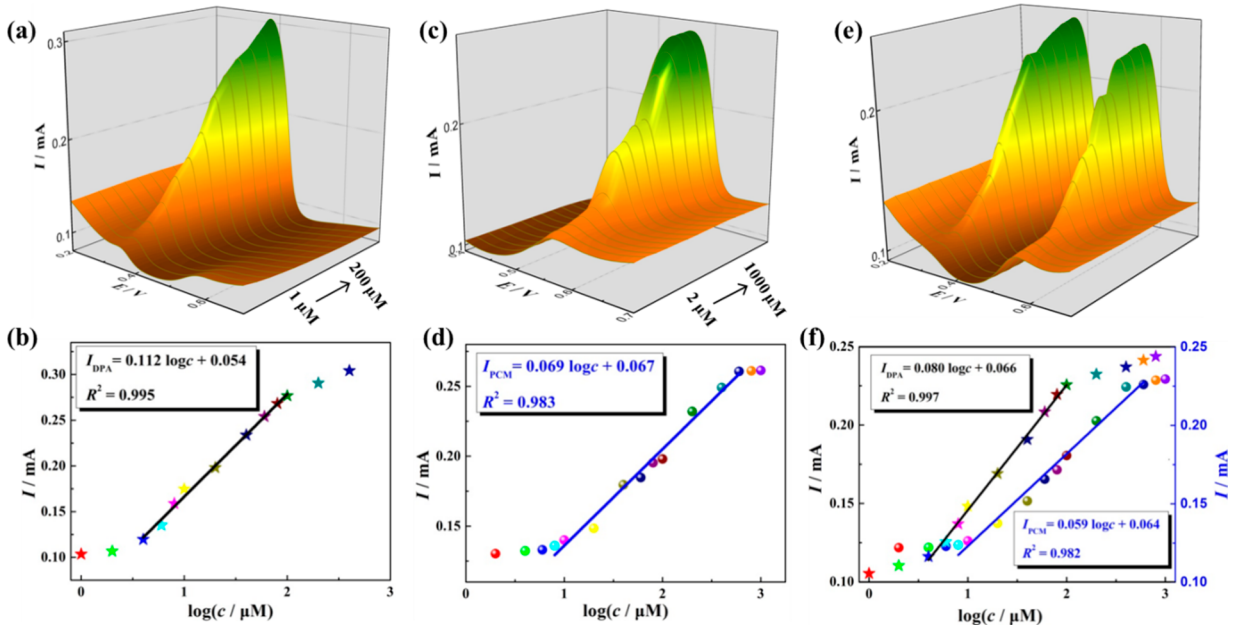

Figure 5. Variations of the DPV peak current intensity for **1**@CFMCN/GCE ECS in 0.1 M NaH_2PO_4–Na_2HPO_4 solution (pH 3.0) containing different concentrations of (a) DPA (from 1 to 200 μM), (c) PCM (from 2 to 1000 μM), and (e) both DPA (from 1 to 800 μM) and PCM (from 2 to 1000 μM). The relations of the DPV peak current for the **1**@CFMCN/GCE ECS versus the logarithm of different concentrations of (b) DPA (4–100 μM), (d) PCM (8–600 μM), and (f) both DPA (4–100 μM) and PCM (8–600 μM).

potentials move slightly in the negative direction while the anodic peak potentials move slightly in the positive direction, and this phenomenon states a reversible but nonideal redox process. On the other hand, the oxidation and reduction peak currents of DPA and PCM simultaneously increase with increases in the scan rate, and the good linear relationship between the peak currents and the scan rate implies that the electrochemical redox processes of DPA and PCM for the **1**@CFMCN/GCE ECS are surface-controlled.[62,69]

Compared with the CV method, DPV is often considered to be a more sensitive method for detecting small molecules because intensive signals could be gained by banishing the

https://dx.doi.org/10.1021/acs.inorgchem.0c02318
Inorg. Chem. 2020, 59, 15355–15364

non-Faradaic currents that exist in the CV method.[64] Hence, DPV was also chosen to explore the relationship between the concentration of DPA and PCM and the peak current (Figure 5). In the individual dectction of DPA and PCM, the DPV peak potentials of DPA or PCM for the **1**@CFMCN/GCE ECS in 0.1 M NaH_2PO_4–Na_2HPO_4 (pH 3.0) solution appear at 0.380 and 0.560 V, respectively. As presented in Figure 5a, when the DPA concentration changes from 1 to 200 μM, the DPV peak current intensity increases gradually. The linear relationship between the peak current and the logarithm of the DPA concentration (4−100 μM) can be fitted by the regression equation of I_{DPA} (mA) = 0.112 × log c (μM) + 0.054 (R^2 = 0.995) (Figure 5b). The limit of detection (LOD) is 0.038 μM, which is acquired from 3s (s: standard deviation) divided by the slope of the linear part (k). The s value is calculated from three blank current measurements without DPA. In the same way, the variation of the DPV peak current intensity with the PCM concentration (2−1000 μM) was also recorded, and a similar tendency can be observed in which the PCM peak current increases with the enhancement of concentration (Figure 5c). The calibration plot shows a linear relationship between the DPV peak current and the concentration of PCM ranging from 8 to 600 μM (Figure 5d). The linear regression equation is I_{PCM} (mA) = 0.069 × log c (μM) + 0.067 (R^2 = 0.995), and the LOD is 1.74 μM. The results above demonstrate that the **1**@CFMCN/GCE ECS could potentially be applied as a promising sensor to detect DPA or PCM and further provides a possibility that DPA and PCM could be simultaneously detected in their mixed solution.

The peak current changes in DPA and PCM with simultaneously increasing concentrations of two analytes were studied (Figure 5e). It is clear that two separated oxidation signals arise with the concentrations increasing from 1 to 800 μM for DPA and 2 to 1000 μM for PCM. The peak currents exhibit the linear correlation to the concentration in the range of 4−100 μM for DPA and 8−600 μM for PCM, and their corresponding regression equations are I_{DPA} (mA) = 0.080 × log c (μM) + 0.066 (R^2 = 0.997) and I_{PCM} (mA) = 0.059 × log c (μM) + 0.064 (R^2 = 0.982) with LODs of 0.053 and 2.03 μM for DPA and PCM (Figure 5f). Besides the detecting scope and the LOD, the oxidation potentials and peak currents of DPA and PCM in the simultaneous detection are similar to those in the individual detection, which provides evidence that the coexistence of DPA and PCM does not influence the sensing performance. Therefore, the **1**@CFMCN/GCE ECS could be effectively utilized as an ECS to simultaneously detect DPA and PCM.

Additionally, the time-dependent stability and the reproducibility of the **1**@CFMCN/GCE ECS were also examined by means of DPV tests in 0.1 M NaH_2PO_4–Na_2HPO_4 (pH 3.0) containing 50 μM DPA and 50 μM PCM (Figures S14 and S15). As illustrated in Figure S14, the DPV peak currents are barely changed for 7 days, which reveal that the **1**@CFMCN/GCE ECS has good stability in detect DPA and PCM. In order to investigate the reproducibility, five independent **1**@CFMCN/GCE ECSs were fabricated to test the concentration of DPA and PCM (Figure S15). The DPV peak currents for these five tests are very close, and the relative standard deviations of DPA and PCM are 2.92 and 1.21%, which exhibit acceptable reproducibility of the **1**@CFMCN/GCE ECS.

CONCLUSIONS

An organic−inorganic cerium-encapsulated SeT hybrid **1** comprising three POM subunits was acquired in the acetic acid and aqueous mixed solution. Its POA is made up of Ce−W−Se heterometal cluster $\{Ce_6Se_2W_{15}\}$ connecting four trilacunary $[B\text{-}\alpha\text{-}SeW_9O_{33}]^{8-}$ segments. The rare $\{Se_2W_7\}$ subunit was observed, in which the central W atom together with two triangular triads formed by three edge-sharing $\{WO_6\}$ octahedra are aligned in the dumbbell-shaped motif, and two Se^{IV} atoms cap two sides of the W_7 plane in the asymmetrical mode. Moreover, the **1**@CFMCN composite was manufactured by simply using ultrasound on **1** and CFMCN, which was used as the electrode material for constructing the **1**@CFMCN/GCE ECS. The experiments have proven that this ECS exhibits an enhanced current response for DPA and PCM. In the simultaneous detection of DPA and PCM, the broad linear range of concentration of 4−100 μM had an LOD of 0.053 μM for DPA and a linear range of concentration of 8−600 μM with an LOD of 2.03 μM for PCM. In conclusion, this work not only enriches the structural types of organic−inorganic hybrid SeTs with several kinds of POM building blocks and also provides an inspiration to construct complicated Ln-incorporated POMs by innovative synthesis methods but also can exploit and expand electrochemical biosensing applications of POM-based composite materials.

ASSOCIATED CONTENT

Supporting Information

The Supporting Information is available free of charge at https://pubs.acs.org/doi/10.1021/acs.inorgchem.0c02318.

Crystal data, experiments, PXRD, TG, IR, CV, and DPV relevant figures (PDF)

Accession Codes

CCDC 2021004 contains the supplementary crystallographic data for this article. These data can be obtained free of charge via www.ccdc.cam.ac.uk/data_request/cif, or by emailing data_request@ccdc.cam.ac.uk, or by contacting The Cambridge Crystallographic Data Centre, 12 Union Road, Cambridge CB2 1EZ, UK; fax: +44 1223 336033.

AUTHOR INFORMATION

Corresponding Authors

Lijuan Chen − *Henan Key Laboratory of Polyoxometalate Chemistry, College of Chemistry and Chemical Engineering, Henan University, Kaifeng, Henan 475004, People's Republic of China;* orcid.org/0000-0001-5894-2082; Email: ljchen@henu.edu.cn

Junwei Zhao − *Henan Key Laboratory of Polyoxometalate Chemistry, College of Chemistry and Chemical Engineering, Henan University, Kaifeng, Henan 475004, People's Republic of China;* orcid.org/0000-0002-7685-1309; Email: zhaojunwei@henu.edu.cn

Authors

Jun Jiang − *Henan Key Laboratory of Polyoxometalate Chemistry, College of Chemistry and Chemical Engineering, Henan University, Kaifeng, Henan 475004, People's Republic of China*

Lulu Liu − *Henan Key Laboratory of Polyoxometalate Chemistry, College of Chemistry and Chemical Engineering, Henan University, Kaifeng, Henan 475004, People's Republic of China*

https://dx.doi.org/10.1021/acs.inorgchem.0c02318
Inorg. Chem. 2020, 59, 15355−15364

Guoping Liu − *Henan Key Laboratory of Polyoxometalate Chemistry, College of Chemistry and Chemical Engineering, Henan University, Kaifeng, Henan 475004, People's Republic of China*

Dan Wang − *Henan Key Laboratory of Polyoxometalate Chemistry, College of Chemistry and Chemical Engineering, Henan University, Kaifeng, Henan 475004, People's Republic of China*

Yan Zhang − *Henan Key Laboratory of Polyoxometalate Chemistry, College of Chemistry and Chemical Engineering, Henan University, Kaifeng, Henan 475004, People's Republic of China*

Complete contact information is available at: https://pubs.acs.org/10.1021/acs.inorgchem.0c02318

Notes

The authors declare no competing financial interest.

■ ACKNOWLEDGMENTS

This work was supported by the Natural Science Foundation of China (21871077, 21571048, 21671054, 21771052, and 22071042), the Program for Innovation Teams in Science and Technology in Universities of Henan Province (20IRTSTHN004), and the First-Class Discipline Cultivation Project of Henan University (2019YLZDYJ02 and CJ1205A0240019).

■ REFERENCES

(1) Zheng, S. T.; Yang, G. Y. Recent advances in paramagnetic-TM-substituted polyoxometalates (TM = Mn, Fe, Co, Ni, Cu). *Chem. Soc. Rev.* **2012**, *41*, 7623−7646.

(2) Zhan, C.-H.; Zheng, Q.; Long, D.-L.; Vilà-Nadal, L.; Cronin, L. Controlling the reactivity of the $[P_8W_{48}O_{184}]^{40-}$ inorganic ring and its assembly into POMZite inorganic fameworks with silver ions. *Angew. Chem., Int. Ed.* **2019**, *58*, 17282−17286.

(3) Zhao, J. W.; Li, Y. Z.; Chen, L. J.; Yang, G. Y. Research progress on polyoxometalate-based transition-metal rare-earth heterometallic derived materials: synthetic strategies, structural overview and functional applications. *Chem. Commun.* **2016**, *52*, 4418−4445.

(4) Liu, J. C.; Han, Q.; Chen, L. J.; Zhao, J. W.; Streb, C.; Song, Y. F. Aggregation of giant cerium-bismuth tungstate clusters into a 3D porous framework with high proton conductivity. *Angew. Chem., Int. Ed.* **2018**, *57*, 8416−8420.

(5) Kortz, U.; Müller, A.; Slageren, J. V.; Schnack, J.; Dalal, N. S.; Dressel, M. Polyoxometalates: fascinating structures, unique magnetic properties. *Coord. Chem. Rev.* **2009**, *253*, 2315−2327.

(6) Oms, O.; Dolbecq, A.; Mialane, P. Diversity in structures and properties of 3d-incorporating polyoxotungstates. *Chem. Soc. Rev.* **2012**, *41*, 7497−7536.

(7) Ma, X.; Li, H. L.; Chen, L. J.; Zhao, J. W. The main progress over the past decade and future outlook on high-nuclear transition-metal substituted polyoxotungstates: from synthetic strategies, structural features to functional properties. *Dalton Trans.* **2016**, *45*, 4935−4960.

(8) Kozhevnikov, I. V. Catalysis by heteropoly acids and multicomponent polyoxometalates in liquid-phase reactions. *Chem. Rev.* **1998**, *98*, 171−198.

(9) Li, Y. Z.; Luo, J.; Chen, L. J.; Zhao, J. W. Recent progress in metal-functionalized germanotungstates: from structures to properties. *RSC Adv.* **2014**, *4*, 50679−50692.

(10) Fang, X. K.; Kögerler, P.; Furukawa, Y.; Speldrich, M.; Luban, M. Molecular growth of a core-shell polyoxometalate. *Angew. Chem., Int. Ed.* **2011**, *50*, 5212−5216.

(11) Kikukawa, Y.; Kuroda, Y.; Yamaguchi, K.; Mizuno, N. Diamond-shaped $[Ag_4]^{4+}$ cluster encapsulated by silicotungstate ligands: synthesis and catalysis of hydrolytic oxidation of silanes. *Angew. Chem., Int. Ed.* **2012**, *51*, 2434−2437.

(12) Wassermann, K.; Dickman, M. H.; Pope, M. T. Self-assembly of supramolecular polyoxometalates: the compact, water-soluble heteropolytungstate anion $[As^{III}_{12}Ce^{III}_{16}(H_2O)_{36}W_{148}O_{524}]^{76-}$. *Angew. Chem., Int. Ed. Engl.* **1997**, *36*, 1445−1448.

(13) Kortz, U.; Savelieff, M. G.; Ghali, F. Y. A.; Khalil, L. M.; Maalouf, S. A.; Sinno, D. I. Heteropolymolybdates of As^{III}, Sb^{III}, Bi^{III}, Se^{IV}, and Te^{IV} functionalized by amino acids. *Angew. Chem., Int. Ed.* **2002**, *41*, 4070−4073.

(14) Li, H. L.; Liu, Y. J.; Liu, J. L.; Chen, L. J.; Zhao, J. W.; Yang, G. Y. Structural transformation from dimerization to tetramerization of serine-decorated rare-earth-incorporated arsenotungstates induced by the usage of rare-earth salts. *Chem. - Eur. J.* **2017**, *23*, 2673−2689.

(15) Gao, J.; Yan, J.; Mitchell, S. G.; Miras, H. N.; Boulay, A. G.; Long, D. L.; Cronin, L. Self-assembly of a family of macrocyclic polyoxotungstates with emergent material properties. *Chem. Sci.* **2011**, *2*, 1502−1508.

(16) Zhao, J. W.; Li, H. L.; M, X.; Xie, Z. G.; Chen, L. J.; Zhu, Y. S. Lanthanide-connecting and lone-electron-pair active trigonal-pyramidal-AsO_3 inducing nanosized poly(polyoxotungstate) aggregates and their anticancer activities. *Sci. Rep.* **2016**, *6*, 26406−26418.

(17) Xu, X.; Chen, Y. H.; Zhang, Y.; Liu, Y. F.; Chen, L. J.; Zhao, J. W. Rare-earth and antimony-oxo clusters simultaneously connecting antimonotungstates comprising divacant and tetravacant Keggin fragments. *Inorg. Chem.* **2019**, *58*, 11636−11648.

(18) Li, H. L.; Liu, Y. J.; Zheng, R.; Chen, L. J.; Zhao, J. W.; Yang, G. Y. Trigonal pyramidal $\{AsO_2(OH)\}$ bridging tetranuclear rare-earth encapsulated polyoxotungstate aggregates. *Inorg. Chem.* **2016**, *55*, 3881−3893.

(19) Zhou, Z.; Zhang, D. D.; Yang, L.; Ma, P. T.; Si, Y. N.; Kortz, U.; Niu, J. Y.; Wang, J. P. Nona-copper(ii)-containing 18-tungsto-8-arsenate(iii) exhibits antitumor activity. *Chem. Commun.* **2013**, *49*, 5189−5191.

(20) Kortz, U.; Al-Kassem, N. K.; Savelieff, M. G.; Al-Kadi, N. A.; Sadakane, M. Synthesis and characterization of copper-, zinc-, manganese-, and cobalt-substituted dimeric heteropolyanions, $[(\alpha\text{-}XW_9O_{33})_2M_3(H_2O)_3]^{n-}$ (n = 12, X = As^{III}, Sb^{III}, M = Cu^{2+}, Zn^{2+}; n = 10, X = Se^{IV}, Te^{IV}, M = Cu^{2+}) and $[(\alpha\text{-}AsW_9O_{33})_2WO(H_2O)\text{-}M_2(H_2O)_2]^{10-}$ (M = Zn^{2+}, Mn^{2+}, Co^{2+}). *Inorg. Chem.* **2001**, *40*, 4742−4749.

(21) Kortz, U.; Savelieff, M. G.; Bassil, B. S.; Keita, B.; Nadjo, L. Synthesis and characterization of iron(III)-substituted, dimeric polyoxotungstates, $[Fe_4(H_2O)_{10}(\alpha\text{-}XW_9O_{33})_2]^{n-}$ (n = 6, X = As^{III}, Sb^{III}; n = 4, X = Se^{IV}, Te^{IV}). *Inorg. Chem.* **2002**, *41*, 783−789.

(22) Yan, J.; Long, D. L.; Cronin, L. Development of a building block strategy to access gigantic nanoscale heteropolyoxotungstates by using SeO_3^{2-} as a template linker. *Angew. Chem., Int. Ed.* **2010**, *49*, 4117−4120.

(23) Kalinina, I. V.; Peresypkina, E. V.; Izarova, N. V.; Nkala, F. M.; Kortz, U.; Kompankov, N. B.; Moroz, N. K.; Sokolov, M. N. Cyclic tungstoselenites based on $\{Se_2W_{12}\}$ units. *Inorg. Chem.* **2014**, *53*, 2076−2082.

(24) Cameron, J. M.; Gao, J.; Vilà-Nadal, L.; Long, D. L.; Cronin, L. Formation, self-assembly and transformation of a transient selenotungstate building block into clusters, chains and macrocycles. *Chem. Commun.* **2014**, *50*, 2155−2157.

(25) Chen, W. C.; Yan, L. K.; Wu, C. X.; Wang, X. L.; Shao, K. Z.; Su, Z. M.; Wang, E. B. Assembly of Keggin-/Dawson-type polyoxotungstate clusters with different metal units and SeO_3^{2-} heteroanion templates. *Cryst. Growth Des.* **2014**, *14*, 5099−5110.

(26) Gao, J.; Yan, J.; Beeg, S.; Long, D. L.; Cronin, L. One-pot versus sequential reactions in the self-assembly of gigantic nanoscale polyoxotungstates. *J. Am. Chem. Soc.* **2013**, *135*, 1796−1805.

(27) Cameron, J. M.; Gao, J.; Long, D. L.; Cronin, L. Self-assembly and structural transformations of high-nuclearity palladium-rich polyoxometalates. *Inorg. Chem. Front.* **2014**, *1*, 178−185.

(28) Chen, W. C.; Qin, C.; Wang, X. L.; Shao, K. Z.; Su, Z. M.; Wang, E. B. Assembly of Mn-containing unprecedented selenotung-

state clusters with photocatalytic H_2 evolution activity. *Cryst. Growth Des.* **2016**, *16*, 2481−2486.
(29) Yan, J.; Gao, J.; Long, D. L.; Miras, H. N.; Cronin, L. Self-assembly of a nanosized, saddle-shaped, solution-stable polyoxometalate anion built from pentagonal building blocks: $[H_{34}W_{119}Se_8Fe_2O_{420}]^{54-}$. *J. Am. Chem. Soc.* **2010**, *132*, 11410−11411.
(30) Chen, W. C.; Qin, C.; Wang, X. L.; Li, Y. G.; Zang, H. Y.; Jiao, Y. Q.; Huang, P.; Shao, K. Z.; Su, Z. M.; Wang, E. B. Assembly of Fe-substituted Dawson-type nanoscale selenotungstate clusters with photocatalytic H_2 evolution activity. *Chem. Commun.* **2014**, *50*, 13265−13267.
(31) Boskovic, C. Rare earth polyoxometalates. *Acc. Chem. Res.* **2017**, *50*, 2205−2214.
(32) Ritchie, C.; Moore, E. G.; Speldrich, M.; Kögerler, P.; Broskovic, C. Terbium polyoxometalate organic complexes: correlation of structure with luminescence properties. *Angew. Chem., Int. Ed.* **2010**, *49*, 7702−7705.
(33) Wang, D.; Li, Y. M.; Zhang, Y.; Xu, X.; Liu, Y.; Chen, L. J.; Zhao, J. W. Construction of Ln^{3+}-substituted arsenotungstates modified by 2,5-thiophenedicarboxylic acid and application in selective fluorescence detection of Ba^{2+} in aqueous solution. *Inorg. Chem.* **2020**, *59*, 6839−6848.
(34) Fukaya, K.; Yamase, T. Alkali-metal-controlled self-assembly of crown-shaped ring complexes of lanthanide/$[\alpha$-$AsW_9O_{33}]^{9-}$: $[K\subset Eu(H_2O)_2(\alpha$-$AsW_9O_{33})\}_6]^{35-}$ and $[Cs\subset Eu(H_2O)_2(\alpha$-$AsW_9O_{33})\}_4]^{23-}$. *Angew. Chem., Int. Ed.* **2003**, *42*, 654−658.
(35) Hussain, F.; Conrad, F.; Patzke, G. R. A gadolinium-bridged polytungstoarsenate(III) nanocluster: $[Gd_8As_{12}W_{124}O_{432}(H_2O)_{22}]^{60-}$. *Angew. Chem., Int. Ed.* **2009**, *48*, 9088−9091.
(36) Hussain, F.; Gable, R. W.; Speldrich, M.; Kögerler, P.; Boskovic, C. Polyoxotungstate-encapsulated Gd_6 and Yb_{10} complexes. *Chem. Commun.* **2009**, 328−330.
(37) Shang, S. X.; Lin, Z. G.; Yin, A. S.; Yang, S.; Chi, Y. N.; Wang, Y.; Dong, J.; Liu, B.; Zhen, N.; Hill, C. L.; Hu, C. W. Self-assembly of Ln(III)-containing tungstotellurates(VI): correlation of structure and photoluminescence. *Inorg. Chem.* **2018**, *57*, 8831−8840.
(38) Chen, W. C.; Li, H. L.; Wang, X. L.; Shao, K. Z.; Su, Z. M.; Wang, E. B. Assembly of cerium(III)-stabilized polyoxotungstate nanoclusters with SeO_3^{2-}/TeO_3^{2-} templates: from single polyoxoanions to inorganic hollow spheres in dilute solution. *Chem. - Eur. J.* **2013**, *19*, 11007−11015.
(39) Chen, W. C.; Qin, C.; Li, Y. G.; Zang, H. Y.; Shao, K. Z.; Su, Z. M.; Wang, E. B. Assembly of large purely-inorganic Ce-stabilized/bridged selenotungstates: from nanoclusters to layers. *Chem. - Asian J.* **2015**, *10*, 1184−1192.
(40) Yang, L.; Li, L.; Guo, J. P.; Liu, Q. S.; Ma, P. T.; Niu, J. Y.; Wang, J. P. A nanosized gly-decorated praseodymium-stabilized selenotungstate cluster: synthesis, structure, and oxidation catalysis. *Chem. - Asian J.* **2017**, *12*, 2441−2446.
(41) Chen, W. C.; Jiao, C. Q.; Wang, X. L.; Shao, K. Z.; Su, Z. M. Self-assembly of nanoscale Lanthanoid-containing selenotungstates: synthesis, structures, and magnetic studies. *Inorg. Chem.* **2019**, *58*, 12895−12904.
(42) Li, H. L.; Yang, W.; Chai, Y.; Chen, L. J.; Zhao, J. W. A novel Dawson-like cerium(IV)-hybridizing selenotungstate $Na_{13}H_7[Ce(SeW_{17}O_{59})_2]\cdot 31\ H_2O$. *Inorg. Chem. Commun.* **2015**, *56*, 35−40.
(43) Liu, Y. J.; Li, H. L.; Lu, C. T.; Gong, P. J.; Ma, X. Y.; Chen, L. J.; Zhao, J. W. Organocounterions-assisted and pH-controlled self-assembly of five nanoscale high-nuclear lanthanide substituted heteropoly-tungstates. *Cryst. Growth Des.* **2017**, *17*, 3917−3928.
(44) Li, H. L.; Liu, Y. J.; Li, Y. M.; Chen, L. J.; Zhao, J. W.; Yang, G. Y. Unprecedented selenium and lanthanide simultaneously bridging selenotungstate aggregates stabilized by four tetra-vacant Dawson-like $\{Se_2W_{14}\}$ units. *Chem. - Asian J.* **2018**, *13*, 2897−2907.
(45) Li, H. L.; Lian, C.; Chen, L. J.; Zhao, J. W.; Yang, G. Y. Two Ce^{3+}-substituted selenotungstates regulated by *N*,*N*-dimethylethanolamine and dimethylamine hydrochloride. *Inorg. Chem.* **2019**, *58*, 8442−8450.
(46) Zhang, Y.; Li, Y. J.; Pang, J. J.; Liu, Y. F.; Li, P.; Chen, L. J.; Zhao, J. W. Two penta-RE^{III} encapsulated tetravacant dawson selenotungstates and nanoscale derivatives and their luminescence properties. *Inorg. Chem.* **2019**, *58*, 7078−7090.
(47) Reinoso, S.; Giménez-Marqués, M.; Galán-Mascarós, J. R.; Vitoria, P.; Gutiérrez-Zorrilla, J. M. Giant crown-shaped polytungstate formed by self-assembly of Ce^{III}-stabilized dilacunary Keggin fragments. *Angew. Chem., Int. Ed.* **2010**, *49*, 8384−8388.
(48) Bassil, B. S.; Dickman, M. H.; Römer, I.; Kammer, B. V. D.; Kortz, U. The tungstogermanate $[Ce_{20}Ge_{10}W_{100}O_{376}(OH)_4(H_2O)_{30}]^{56-}$: a polyoxometalate containing 20 Cerium(III) atoms. *Angew. Chem., Int. Ed.* **2007**, *46*, 6192−6195.
(49) Liu, J. L.; Jin, M. T.; Chen, L. J.; Zhao, J. W. First dimethyltin-functionalized rare-earth incorporated tellurotungstates consisting of $\{B$-α-$TeW_7O_{28}\}$ and $\{W_5O_{18}\}$ mixed building units. *Inorg. Chem.* **2018**, *57*, 12509−12520.
(50) Bi, L. H.; Dickman, M. H.; Kortz, U.; Dix, I. The Ru(II)-supported heptatungstates $[HXW_7O_{28}Ru(dmso)_3]^{6-}$ (X = P, As). *Chem. Commun.* **2005**, 3962−3964.
(51) Martín-Caballero, J.; Artetxe, B.; Reinoso, S.; Felices, L. S.; Castillo, O.; Beobide, G.; Vilas, J. L.; Gutiérrez-Zorrilla, J. M. Thermally-triggered crystal dynamics and permanent porosity in the first heptatungstate-metalorganic three-dimensional hybrid framework. *Chem. - Eur. J.* **2017**, *23*, 14962−14974.
(52) Clemente-Juan, J. M.; Coronado, E.; Forment-Aliaga, A.; Galán-Mascarós, J. R.; Giménez-Saiz, C.; Gómez-García, C. J. A new heptanuclear Cobalt(II) cluster encapsulated in a novel heteropolyoxometalate topology: synthesis, structure, and magnetic properties of $[Co_7(H_2O)_2(OH)_2P_2W_{25}O_{94}]^{16-}$. *Inorg. Chem.* **2004**, *43*, 2689−2694.
(53) Fisher, F. C.; Hacinga, E. Thermal and photoinduced deboronations of some pyridine- and benzeneboronate anions. *Recl. Trav. Chim. Pays-bas* **1974**, *93*, 21−24.
(54) Bahadır, E. B.; Sezgintürk, M. K. Electrochemical biosensors for hormone analyses. *Biosens. Bioelectron.* **2015**, *68*, 62−71.
(55) Alam, A. U.; Qin, Y. H.; Howlader, M. M. R.; Hu, N. X.; Deen, M. J. Electrochemical sensing of acetaminophen using multi-walled carbon nanotube and β-cyclodextrin. *Sens. Actuators, B* **2018**, *254*, 896−909.
(56) Martín, A.; Vázquez, L.; Escarpa, A. Carbon nanomaterial scaffold films with conductivity at micro and sub-micron levels. *J. Mater. Chem. A* **2016**, *4*, 13142−13147.
(57) Ryu, Y.; Freeman, D.; Yu, C. High electrical conductivity and *n*-type thermopower from double-/single-wall carbon nanotubes by manipulating charge interactions between nanotubes and organic/inorganic nanomaterials. *Carbon* **2011**, *49*, 4745−4751.
(58) Song, Z. M.; Wang, L.; Chen, N.; Cao, A.; Liu, Y. F.; Wang, H. F. Biological effects of agglomerated multi-walled carbon nanotubes. *Colloids Surf., B* **2016**, *142*, 65−73.
(59) Dolbecq, A.; Dumas, E.; Mayer, C. R.; Mialane, P. Hybrid organic- inorganic polyoxometalate compounds: from structural diversity to applications. *Chem. Rev.* **2010**, *110*, 6009−6048.
(60) Liu, M. L.; Chen, Q.; Lai, C. L.; Zhang, Y. Y.; Deng, J. H.; Li, H. T.; Yao, S. Z. A double signal amplification platform for ultrasensitive and simultaneous detection of ascorbic acid, dopamine, uric acid and acetaminophen based on a nanocomposite of ferrocene thiolate stabilized Fe_3O_4@Au nanoparticles with graphene sheet. *Biosens. Bioelectron.* **2013**, *48*, 75−81.
(61) Jiang, J. J.; Du, X. Z. Sensitive electrochemical sensors for simultaneous determination of ascorbic acid, dopamine, and uric acid based on Au@Pd-reduced graphene oxide nanocomposites. *Nanoscale* **2014**, *6*, 11303−11309.
(62) Alam, A. U.; Qin, Y. H.; Catalano, M.; Wang, L. H.; Kim, M. J.; Howlader, M. M. R.; Hu, N. X.; Deen, M. J. Tailoring MWCNTs and β-cyclodextrin for sensitive detection of acetaminophen and estrogen. *ACS Appl. Mater. Interfaces* **2018**, *10*, 21411−21427.
(63) Su, C. L.; Li, Z. Y.; Zhang, D.; Wang, Z. M.; Zhou, X.; Liao, L. F.; Xiao, X. L. A highly sensitive sensor based on a computer-designed

https://dx.doi.org/10.1021/acs.inorgchem.0c02318
Inorg. Chem. 2020, 59, 15355−15364

magnetic molecularly imprinted membrane for the determination of acetaminophen. *Biosens. Bioelectron.* **2020**, *148*, 111819−111826.
(64) Rajamani, A. R.; Peter, S. C. Novel nanostructured Pt/CeO_2 @ Cu_2O carbon-based electrode to magnify the electrochemical detection of theneurotransmitter dopamine and analgesic paracetamol. *ACS Appl. Nano Mater.* **2018**, *1*, 5148−5157.
(65) Alothman, Z. A.; Bukhari, N. S.; Wabaidur, M.; Haider, S. Simultaneous electrochemical determination of dopamine and acetaminophen using multiwall carbon nanotubes modified glassy carbon electrode. *Sens. Actuators, B* **2010**, *146*, 314−320.
(66) Zhou, D.; Han, B. H. Graphene-based nanoporous materials assembled by mediation of polyoxometalate nanoparticles. *Adv. Funct. Mater.* **2010**, *20*, 2717−2722.
(67) Yokuş, Ö. A.; Kardaş, F.; Akyıldırım, O.; Eren, T.; Atar, N.; Yola, M. L. Sensitive voltammetric sensor based on polyoxometalate /reduced graphene oxide nanomaterial: application to the simultaneous determination of L-tyrosine and L-tryptophan. *Sens. Actuators, B* **2016**, *233*, 47−54.
(68) Bai, Z. Y.; Zhou, C. L.; Xu, H. B.; Wang, G. N.; Pang, H. J.; Ma, H. Y. Polyoxometalates-doped Au nanoparticles and reduced grapheme oxide: A new material for the detection of uric acid in urine. *Sens. Actuators, B* **2017**, *243*, 361−371.
(69) Alam, A. U.; Qin, Y. H.; Howlade, M. M. R.; Hu, N. X.; Deen, M. J. Electrochemical sensing of acetaminophen using multi-walled carbon nanotube and β-cyclodextrin. *Sens. Actuators, B* **2018**, *254*, 896−909.

https://dx.doi.org/10.1021/acs.inorgchem.0c02318
Inorg. Chem. 2020, 59, 15355−15364